SAND2015-10525C

kHz Rate Digital In-line Holography Applied to Quantify Secondary Droplets from the Aerodynamic Breakup of a Liquid Column in a Shock-Tube

Daniel R. Guildenbecher[1], Justin L. Wagner[2], Joseph D. Olles[3],
Ellen Y. Chen[4], Edward P. DeMauro[5], Paul A. Farias[6], Thomas W. Grasser[7]
Sandia National Laboratories, Albuquerque, NM 87185

Paul E. Sojka[8]
Purdue University, West Lafayette, IN 47907

The breakup of liquids due to aerodynamic forces has been widely studied. However, the literature contains limited quantified data on secondary droplet sizes, particularly as a function of time. Here, a column of liquid water is subjected to a step change in relative gas velocity using a shock tube. A unique digital in-line holography (DIH) configuration is proposed which quantifies the secondary droplets sizes, three-dimensional position, and three-component velocities at 100 kHz. Results quantify the detailed evolution of the characteristic mean diameters and droplet size-velocity correlations as a function of distance downstream from the initial location of the water column. Accuracy of the measurements is confirmed through mass balance. These data give unprecedented detail on the breakup process which will be useful improved model development and validation.

I. Introduction

Aerodynamic forces along the surface of a liquid tend to distort the surface, while interfacial surface tension resists this distortion. When aerodynamic forces exceed surface tension forces, the liquid breaks apart into secondary droplets. These physics are crucial to the formation of fuel sprays in engines, liquid dispersion in rain storms, and many other natural and applied phenomena. For these reasons, aerodynamic breakup of liquids has been widely investigated for at least the last century with hundreds of articles published. Recent reviews are provided by Guildenbeher *et. al*[1] and Theofanous[2]. For liquids of low to moderate viscosity, these works indicate that observable breakup morphologies are most strongly correlated to the non-dimensional Weber number,

$$We = \frac{\rho_g u^2 d}{\sigma}, \tag{1}$$

where ρ_g is the gas-phase density, u, is the characteristic gas-to-liquid relative velocity, d is the characteristic liquid dimension, and σ is the interfacial surface tension. For characterization of temporal behavior, time is typically non-dimensionalized by a characteristic transport time,

$$\tau = \frac{tu}{d}\sqrt{\frac{\rho_g}{\rho_l}}, \tag{2}$$

where t is the dimensional time and ρ_l is the liquid density.

---

[1] Senior Member of the Technical Staff, Engineering Sciences Center, drguild@sandia.gov.
[2] Senior Member of the Technical Staff, Engineering Sciences Center
[3] Senior Member of the Technical Staff, Energetic Components Center
[4] Post-Doctoral Appointee, Engineering Sciences Center
[5] Post-Doctoral Appointee, Engineering Sciences Center
[6] Laboratory Support Technologist, Engineering Sciences Center
[7] Laboratory Support Technologist, Engineering Sciences Center
[8] Professor, School of Mechanical Engineering

Despite the large body of work, limited experimental investigations have been performed which quantify secondary droplet sizes and velocities. This is especially true for experimental configurations which utilize well-controlled, step-changes in relative velocity that are amenable to theoretical investigation and modeling. One reason for this lack of data is that widely available drop size and velocity diagnostics are typically either point measurement or line of sight ensemble techniques and are ill-suited to measurement of transient flow statistics.

Digital in-line holography (DIH) is a laser based measurement technique which utilizes a digital sensor to record the diffraction patterns caused by particles in a flow.[3] After recording, digital holograms are numerically refocused to reveal the 3D positions and 2D particle morphologies. With appropriately defined algorithms[4-7], DIH enables automatic quantification of all particles along the line-of-sight and is therefore well suited to rapid quantification of particle statistics[8-10].

Most previous applications of DIH utilize low-speed (~10Hz) image arrays which are advantageous due to their relatively low noise characteristics and high pixel counts. However, as a consequence, investigation of temporal phenomena has been mostly limited to ensemble averaging of repeated experiments[8]. In this work, we discuss our most recent efforts to increase the temporal resolution of DIH using high-speed, kHz rate image arrays. The breakup of a liquid column subject to a step change in relative gas velocity is considered.

II. Experimental Configuration

Experiments are performed in Sandia's Multiphase Sock Tube[11-13]. This facility uses pressurized nitrogen in a driver section along with a fast action valve to propagate a planar shock into a driven section. Before firing of the shock tube, a column of liquid water is established using a low-speed, laminar jet with diameter of approximately 1 mm. One-dimensional convective flow, which follows the shock, creates an approximate step change in relative gas velocity with respect to the water column. Over time, surface instabilities develop and grow non-linearly, leading to breakup of the water column. Fig. 1 shows typical back-lit, high-speed imaging of the process.

Due to out of focus features, accurate measurement of secondary droplet sizes and velocities from white light images, such as Fig. 1, is difficult. To address this, the dual-view DIH configuration shown in Fig. 2 is utilized. The collimated beam from a continuous wave, 532 nm laser is propagated perpendicular through the shock-tube. Diffraction patterns develop as the secondary droplets pass through the laser beam. These are recorded using two high-speed cameras (Photron SA-Z, operating at up to 100 kHz, 250 ns integration time) with optics to record digital holograms with roughly 2× and 6× magnification. By recording at two-separate magnifications, the overall particle size dynamic range is increased.

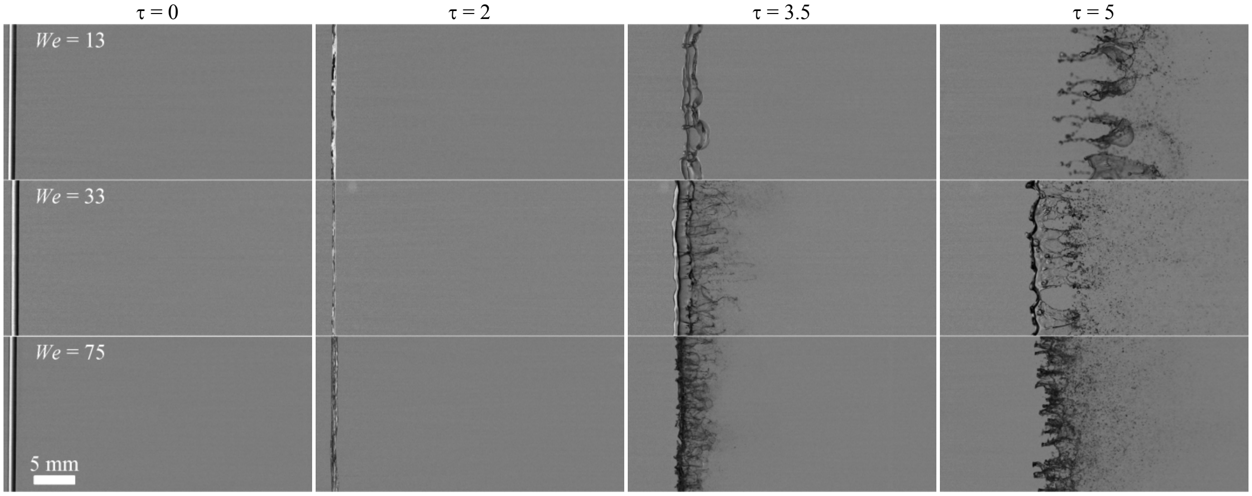

Fig. 1. Typical back-lit high-speed imaging of the breakup process showing the initial laminar water jet before passage of the shock (τ = 0), the jet deformed by the convective flow behind the shock (τ = 2), and the jet breaking up into secondary drops (τ > 2).

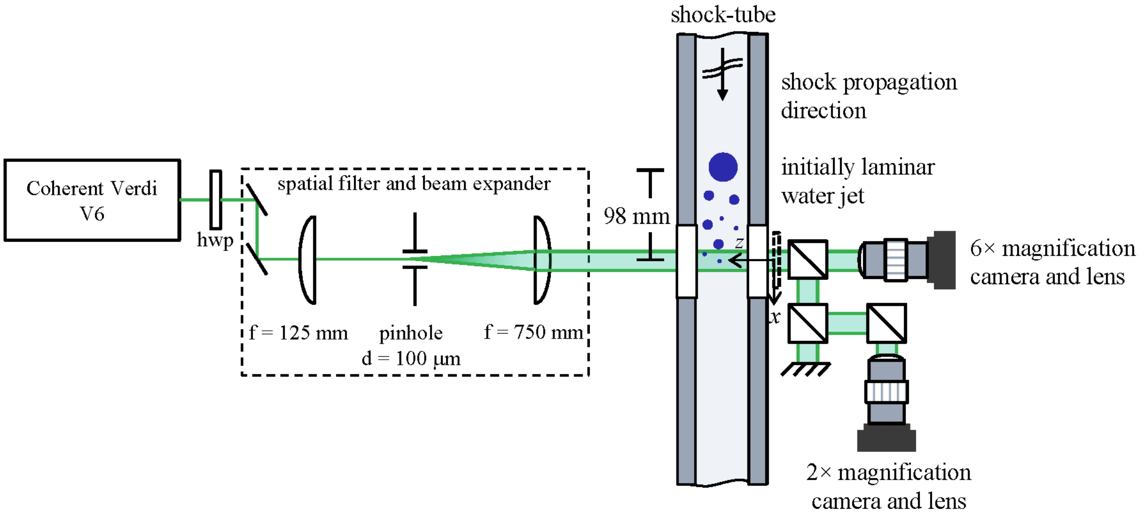

Fig. 2. Experimental configuration illustrating a top-down view of the multiphase shock tube and DIH optics. hwp: half wave plate, bs: 50/50 non-polarizing beam splitter, pbs: polarizing beam splitter

As discussed in Wagner *et al.*[13], the temporal history of the gas velocity in the empty shock tube (without the water column) is quantified using kHz rate particle image velocimetry (PIV). This allows for detailed characterization of the convective flow velocity. Fig. 3 shows typical results taken at approximately the same location as the subsequent DIH experiments. Here, P_4 is the initial absolute pressure of the shock tube driver section. Lines show the mean measured velocity from three realizations, while error bars show the standard deviation. Compared to previous investigations using this facility[11-13], in the current work, the shock tube is operated at relatively low driver pressures. This is necessary to achieve a range of convective flow velocities (Weber numbers) which show distinct variations in breakup morphologies (see Fig. 1). However, as a consequence, the shock tube and fast valve are operated at off-design conditions. Particularly at the lowest pressure, the convective velocity shows a slow ramp rather than the step change expected for an ideal, 1D shock. This is likely due to multiple pressures waves which are released during the opening time of the valve and have not merged into a 1D shock before reaching the test section. While these non-ideal conditions may somewhat complicate modeling of the breakup process, the results in Fig. 3 indicate that the measurements are reproducible and, therefore, could be directly used for boundary conditions in simulations.

After passing through the test section, the shock wave (or pressure waves) travel to the end of the shock tube, reflect off a solid end wall, and eventually return to the test section causing the drop in convective flow velocity at approximately 3.5 ms shown in Fig. 3. In our initial breakup experiments, it was observed that this total test time was too short for completion of breakup at all conditions. To address this, the shock tube was extended before obtaining the DIH results shown in the subsequent section. While detailed PIV measurements have yet to be completed after this modification, wall pressure measurements indicate that the total test time is extended to approximately 5.5 ms during which time the convective velocity remains relatively constant at the plateau levels observed in Fig. 3. For definition of the non-dimensional operating conditions, the characteristic relative velocity, u, is approximately by these plateaus levels. This is summarized in Table 1 where uncertainty is approximated from the standard deviation in the plateau region. Finally, the gas density shown in Table 1 is approximated using 1D shock theory[14] and the measured value of u.

In the current experiment, the water jet is formed from pure, deionized water with assumed interfacial surface tension, $\sigma = 0.072$ N/m and density, $\rho_l = 1000$ kg/m^3. Using the methods described in the next section, the initial jet diameter, d, is quantified from the DIH results recorded before arrival of the shock. This gives a measured initial diameter of $d = 0.94 \pm 0.01$ mm where the uncertainty is taken as the standard deviation of measured diameters from nine experiments. The final column in Table 1 gives the estimated We for the three conditions studied here. Uncertainty in We is determined from the combined uncertainty of the physical quantities using the method outlined in Kline and McClintock[15].

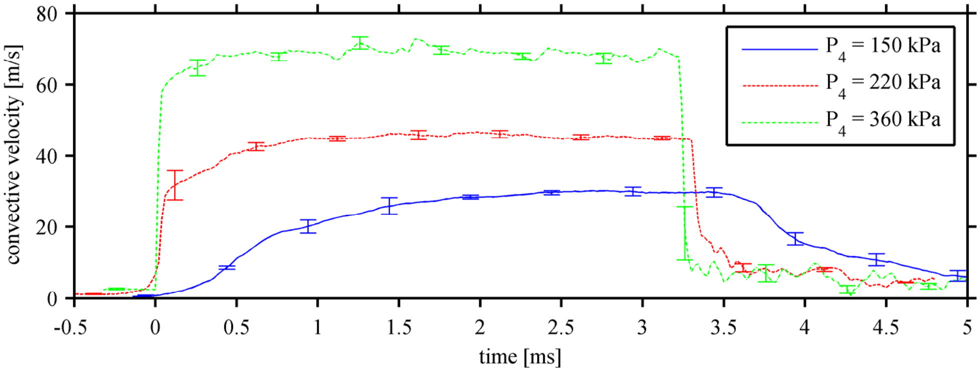

Fig. 3. Mean gas-phase centerline velocities in the streamwise direction for the empty shock tube operated at the specified driver pressures, P_4, quantified using high-speed PIV as outlined in Wagner *et al.*[13]. Solid lines show the mean from three realizations while error bars show the standard deviation.

Table 1. Experimental conditions.

relative gas velocity, u [m/s]	estimated gas density, ρ_g [kg/m^3]	Weber number, We
30 ± 2	1.09	13 ± 2
47 ± 2	1.13	33 ± 3
69 ± 2	1.20	75 ± 4

Most previous investigations of aerodynamic fragmentation consider the breakup of isolated, spherical drops in a cross-flow. While the geometry differs here, it is nevertheless interesting to compare the observed breakup morphologies to those given in the literature on spherical drops[1]. At the lowest $We = 13$, a "bag breakup" morphology is predicted. This is characterized by the formation of a thin-walled bag structure which grows downstream, eventually breaking into many fine drops. Similar morphologies are observed in the first row in Fig. 1. The intermediate $We = 33$ falls near the observed transition between the "bag" morphology and the so called "multimode" morphology, which is characterized by a combination of bag like structures and sheets that form at the periphery. Again, the observed breakup morphology in the second row in Fig. 1 appears to contain both bag and sheet like structures. Finally, the highest $We = 75$ falls within the predicted "sheet-thinning" regime which is characterized by the breakup of thin sheets that form at the periphery. In this case, the morphology observed in the third row in Fig. 1 may again be similar; however, the current imaging configuration does not conclusively reveal where "sheet" structures are forming, and additional evidence is needed to determine if indeed the sheets are forming at the periphery as predicted. Still, taken together these observations indicate that the breakup morphology of a jet in cross-flow is similar to that of a drop in cross-flow. Consequently, much of what is known about the interfacial instabilities that lead to drop breakup can likely be extended to the jet in cross-flow considered here.

III. Results

As discussed in the previous section, DIH videos of the breakup process are recorded at two fields of view; however, for the initial results presented here, only the 2× field of view is considered. Furthermore, only those results for the $We = 33$ case are presented. The top row in Fig. 4 shows example DIH results recorded at 100 kHz on a 640×280 pixel array. Prior to the experiments the exact magnification is determined by imaging a dot grid with known spacing. From this the effective pixel size, $\Delta x = 12.3\text{-}12.9$ µm, is measured. Small variations are due to realignment during the experimental campaign.

As discussed in detail elsewhere[4-6], digital holograms, such as those shown in the top row in Fig. 4, are numerically refocused along the optical depth, z, by solving the diffraction equation,

$$E(x,y;z) = \left[h(x,y)\,E_r^*(x,y)\right] \otimes g(x,y;z). \tag{3}$$

Here, h is the recorded hologram, E is the reconstructed complex amplitude, x, y are the spatial coordinates in the hologram plane, $\otimes$ is the convolution operation, and g is the diffraction kernel. Equation (3) is numerically evaluated to find $E(x, y; z)$ at any z, and the reconstructed light field is visualized using its amplitude, $A = |E|$. For example, the bottom row in Fig. 4 shows the numerically refocused amplitude images at the optical depth of the water jet ($z = 80$ mm). In these images numerous in-focus features can be observed including many secondary droplets as well as the intact portion of the core. These results correspond to a non-dimensional time of $\tau \approx 3.5$ and can be compared with the third column in the middle row in Fig. 1 which was recorded at nominally the same condition. Compared with the white light images in Fig. 1, the DIH results in Fig. 4 are recorded at a higher magnification and therefore reveal more fine features. Furthermore by varying the refocus depth, z, DIH allows for in-focus imaging of all secondary droplets, whereas in the white light images many of the secondary drops appear out of focus. Note, however that DIH is challenged in regions of high particle density and regions with overlapping structures, such as very near the intact jet. There, diffraction by more than one surface causes loss of phase information, making interpretation of the refocused images extremely challenging. For this reason, the remainder of this work focuses on quantification of the secondary droplets in regions away from the intact core.

The 3D position and 2D size of the secondary droplets are automatically measured from each hologram image via application of the processing algorithms defined in our previous works[4-6]. Specifically, the hologram images are numerically refocused to 5001 planes evenly spaced over a range of z-depths found to contain in-focus features. At each depth, the reconstructed amplitude image is thresholded to give a 2D binary image. Regions which potentially contain droplets are connected together to yield a 3D binary image. Segmentation is then used to find the x, y centroid and extent of each connected region. Next, these are used for initial guesses during application of the hybrid method defined in Guildenbecher *et al.*[4] This method automatically determines the optical depth, z, of each particle based on the location where local edge sharpness is maximized. Furthermore, an optimum segmentation threshold is used to extract the 2D shape of each particle at the determined z-location. To minimize detection of false particles and to prevent measurement of the intact core, no region is accepted with area equivalent diameter less than 37 μm or greater than 700 μm.

The above steps give an estimated x, y, z position and diameter for all particles. As discussed in Katz and Sheng[3] the measured z-position in DIH is particularly susceptible to uncertainty due to the limited angular aperture from which individual particles are reconstructed. To improve this and further eliminate false particle measurements, the regression-based multi-frame tracking algorithm (RMT) defined in Guildenbecher and Sojka[16] is applied. This method locates particle trajectories through frame-to-frame matching followed by smoothing via fitting measured positions to simple models of the temporal motion. (Here, x- and y-positions are fit to models which are quadric with respect to time, while z is fit to a linear model.) Individual trajectories, which are likely to originate from the same particle, are stitched together, and the process is repeated until no further connections are found. The final goal of this processing is to track each particle along a single trajectory which spans the entire field of view. If completely successful, all particles would be measured once and only once, ensuring accurate particle statistics.

Fig. 5 shows example results for the hologram images shown in Fig. 4. In these images, circles show the measured area of each particle, while arrows show the in-plane (x, y) velocities quantified with the RMT algorithm. Visual inspection of these images indicates that most of the particles are successfully tracked. Furthermore, as expected, in regions very near the intact core, the method is unable to differentiate individual particles from the dense cloud.

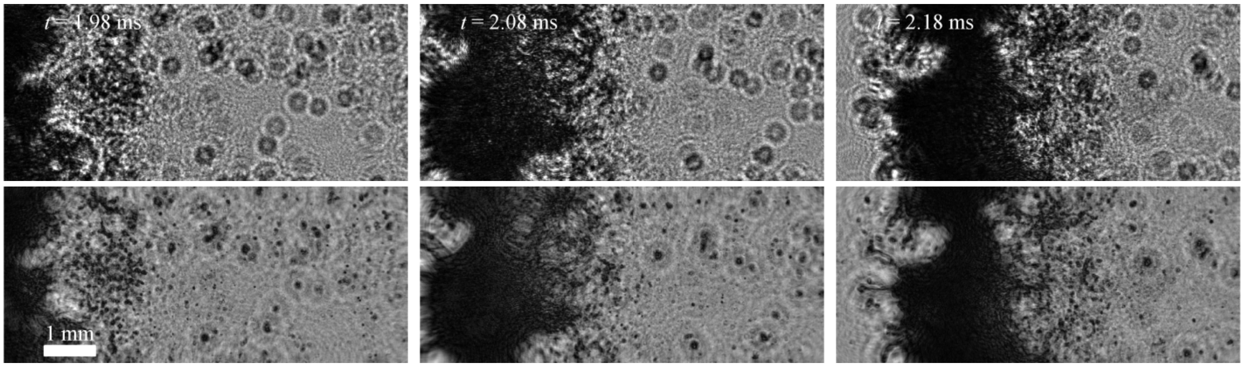

Fig. 4. (top row) Example experimental holograms for *We* = 33 and (bottom row) the corresponding amplitude images which have been numerically refocused to z = 80 mm. The center of the field of view is 12 mm downstream of the initial jet centerline.

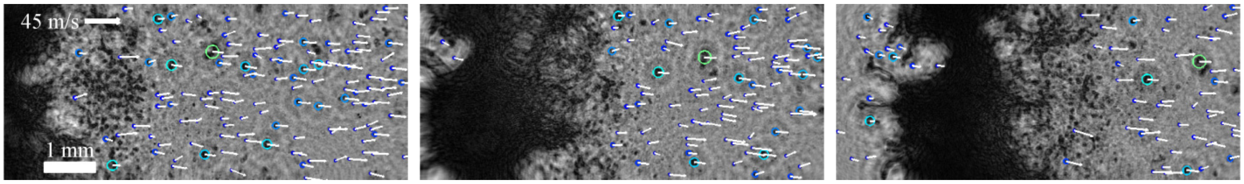

Fig. 5. The measured particle sizes (circles) and in-plane velocities (arrows) for the hologram images shown in Fig. 4.

The results in Fig. 5 show three images from a high-speed video which contains 500 total images. Processing this entire video in the manner described above results in 1224 measured drop trajectories giving the drop size probability density function (pdf) shown in Fig. 6. While the pdf shows the expected tail toward zero at larger diameters, the expected tail toward zero at smaller diameters is not resolved. This is likely due to the limited particle size dynamic range of the current field of view. To better capture the smallest drops, a 6× field of view is also recorded as shown in Fig. 2; however, these data have yet to be fully processed and are not available for the current work. Despite this, to the best of our knowledge, the results in Fig. 5 and Fig. 6 represent the first ever, single-shot quantification of the particle size and velocity statistics from high-speed aerodynamic breakup. We therefore believe this to be a significant advancement in our ability to quantify such flows.

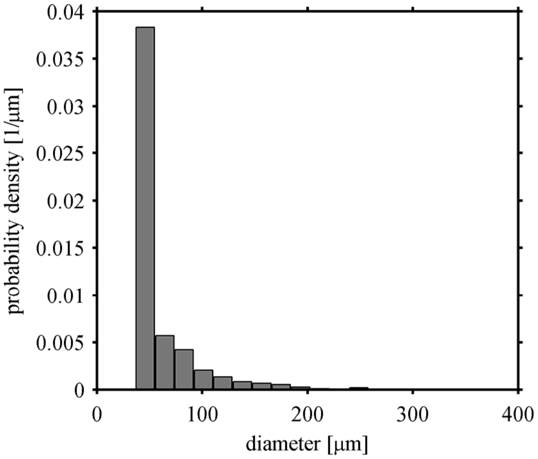

Fig. 6. Drop size probability density function quantified from the high-speed DIH results in Fig. 5.

To further explore the dynamics of the breakup process, the measurement is repeated at multiple locations downstream of the initial jet. This is achieved by fixing the optics in Fig. 2 while translating the water jet upstream. Three high speed DIH videos are recorded at each location and processed in the manner described above. Each video is of sufficient length to record the particles as they enter the field of view, translate through the field and view, and eventually leave. Therefore, every video provides a temporally integrated snapshot of the particle statistics at each downstream location.

Fig. 7(a) shows the total number of drops measured within each field of view. As expected, at further downstream locations the breakup is more complete and the total number of measured drops increases. Perhaps more interestingly, Fig. 7(b) shows the total mass of all measured drops within each field of view. This is calculated by summing the spherical equivalent volume of all droplets and multiplying by ρ_l. In this figure, the dotted line shows the expected total mass of the initial jet which is captured within the vertical extent of the field of view. After complete breakup and assuming all secondary droplets are perfectly measured, the total measured mass should be equal to the total mass of the initial jet. As shown in Fig. 7(b), at the furthest downstream locations, the total measured mass does indeed approach this value. This increases confidence in the measured drop size and velocity statistics reported next. However, it should also be noted that not all potential measurement biases are fully understood. For example, although we attempt to measure the trajectory of all drops once and only once, the measurement is challenged by the relatively high particle number density resulting in observable gaps in some particle trajectories. This effect leads to single particles being counted more than once which results in a positive bias in the total measured mass. On the other hand, as the images in Fig. 5 demonstrate, the relatively high particle number density also causes some secondary drops to be missed entirely. This contributes a negative bias in the total measured mass. It is possible that these two effects counteract one another to some extent, still more work is needed to better understand these biases and their effects on drop size and velocity statistics.

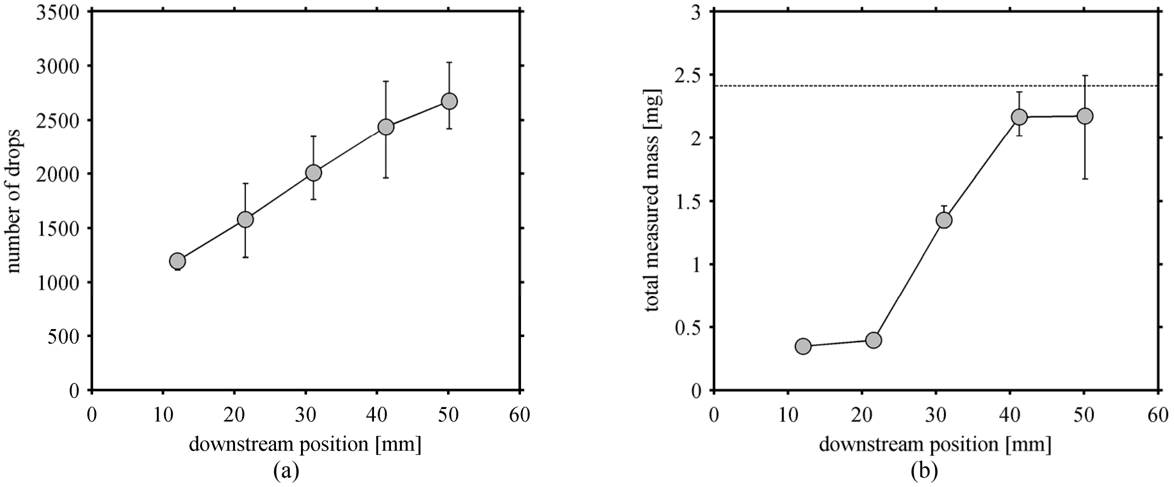

Fig. 7. (a) The total number of secondary drops measured within a field of view centered downstream of the initial jet by the distance shown and (b) the total mass of all measured droplets. Symbols are the mean from three realizations while error bars show the min and max value. In (b) the dotted line shows the total mass of the initial jet captured within the vertical extent of the field of view.

Fig. 8 shows the characteristic mean diameters measured at each downstream location. Here, the characteristic diameters are defined as

$$D_{pq} = \left[\sum d^p \Big/ \sum d^q \right]^{1/(p-q)}, \tag{4}$$

where d is the measured diameter of each drop. As the breakup proceeds downstream, the mean drop sizes tend to increase indicating that larger drops are produced at later times. Furthermore, the spread between the number mean diameter, D_{10}, and the volume, D_{30}, and Sauter mean, D_{32}, diameters tends to increase as the breakup proceeds downstream. Because D_{30} and D_{32} more heavily weight large droplets compared to D_{10}, the increase in the spread between these numbers indicates that the width of the drop size pdf is also increasing downstream.

In contrast to these general trends, the characteristic mean diameters are observed to decrease at the furthest downstream location. This somewhat unexpected result may again be due to unidentified biases. Alternatively, it is possible that at the 41.2 mm location, some of the measured secondary drops are themselves unstable and fragment into smaller drops by the time they reach the furthest downstream location. From the literature on spherical drops, it is well known that isolated drops in a cross-flow are aerodynamically unstable if the relative Weber number, $We \gtrsim 11$.[1] Here, a size and velocity is measured for every drop, and therefore the relative Weber numbers can be determined. These calculations show that at all positions, except the 41.2 mm location, all measured drops have a relative $We < 11$ and therefore are unlikely to breakup further. In contrast, at the 41.2 mm location a number of the measured drops have a relative $We > 11$, indicating they are likely to breakup if they enter an area where local gas velocity is equal to the convective velocity given in Table 1. It is possible that between 41.2 mm to 50.1 mm, a majority of the remaining intact core breaks apart such that these drops escape the relatively low gas velocities in the wake and breakup in this manner. Interestingly, if the mean characteristic diameters are calculated from only those particles with $We < 11$ (open symbols in Fig. 8) then the hump at 41.2 mm is eliminated giving the expected trend of increasing mean diameters with increasing downstream location. Again, this appears to support they hypothesis that the largest drops measured at 41.2 mm have undergone additional fragmentation before reaching the furthest downstream locations. If correct, these findings would provide a physical justification for the modeling of complex fragmentation as a cascade processes initiated when liquid regions experience a relative $We \gtrsim 11$.[17]

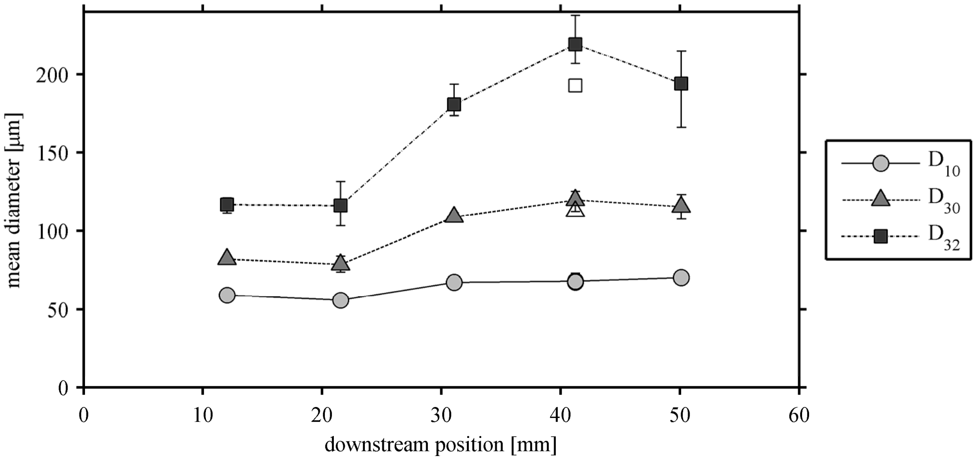

Fig. 8. The characteristic mean diameters measured at each downstream location. Symbols are the mean from three realizations while error bars show the min and max value. Open symbols at 41.2 mm are the characteristic mean diameters calculated from all measured drops with relative *We* < 11.

Finally, Fig. 9 summarized the measured size-velocity correlations in each field of view. Symbols represent the mean streamwise (*x*-direction) velocity for all drops with measured diameter within ± 25 µm of the indicated diameter. As expected, the smallest drops are accelerated more quickly by the local gas velocity and therefore display the highest mean velocities. Furthermore, as breakup precedes downstream, the mean velocities generally increase. The most rapid accelerations are observed between 12 mm to 21.6 mm and again between 41.2 to 50.1 mm. The acceleration at upstream locations (12 to 21.6 mm) may be representative of the time required for the initial drops to accelerate to the gas velocities within the wake behind the intact core. Between 21.6 to 41.2 mm, droplet velocities remain relatively constant perhaps because a majority of drops remain within the wake behind the intact core. Finally, between 41.2 mm to 50.1 mm, the droplets once again experience significant acceleration. It is hypothesized that this is due to breakup of the intact core leading to local gas velocities which approach mean convective velocity given in Table 1.

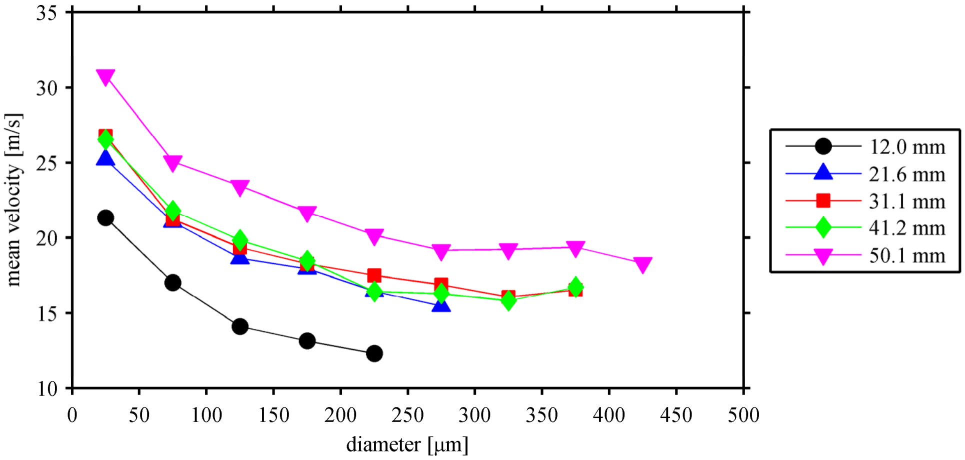

Fig. 9. The average size-velocity correlation at each downstream location. The symbol is the average streamwise velocity for all measured drops with diameter ± 25 µm of the indicated diameter. Only those data points are shown whose average is constructed from at minimum 10 measured drops.

IV. Conclusion

This work presents an experimental investigation of the aerodynamic breakup of a column of liquid water subjected to a step change in relative gas velocity. For the first time, high-speed digital in-line holography (DIH) enables quantification of the secondary droplet size and velocity statistics from single shot experiments. These results are expected to be useful for development and validation of breakup models and simulations. Specific findings include:

- With current technology digital in-line holograms can be recorded at 100 kHz with sufficient spatial resolution to enable 3D measurement of particle position and sizes.
- Favorable comparison of the total measured particle mass to the initial mass of the liquid jet appears to confirm the accuracy of the DIH measurement and the ability to quantify the vast majority of particles within the 3D measurement volume, although more work is needed to fully explore potential measurement biases.
- As breakup progresses downstream the characteristic mean diameters tend to increase, indicating the production of larger secondary drops at later times.
- A unique dip in the characteristic mean diameters is observed at the far downstream positions. Analysis of the local droplet Weber numbers indicates that this dip may be due to the breakup of droplets which are unstable in the local relative gas velocity.
- Particle velocities experience a distinct acceleration at far downstream locations. This may correspond to breakup of the intact core which causes gas acceleration in the region previously containing the wake.

To follow-on from this work, we plan to quantify the high-speed DIH results at the additional conditions mentioned in Table 1. In addition, results from the higher magnification field of view will be explored for extension of the measurable drop size dynamic range. Once complete, the result will be a unique dataset for detailed physical investigation of this fundamental breakup process.

Acknowledgments

Sandia National Laboratories is a multiprogram laboratory operated by Sandia Corporation, a Lockheed Martin Company, for the United States Department of Energy's National Nuclear Security Administration under contract No. DE-AC04-94AL85000.

References

[1]Guildenbecher, D., López-Rivera, C., and Sojka, P. "Secondary atomization," *Experiments in Fluids* Vol. 46, No. 3, 2009, pp. 371-402.

[2]Theofanous, T. G. "Aerobreakup of Newtonian and Viscoelastic Liquids," *Annual Review of Fluid Mechanics* Vol. 43, No. 1, 2011, pp. 661-690.

[3]Katz, J., and Sheng, J. "Applications of holography in fluid mechanics and particle dynamics," *Annual Review of Fluid Mechanics* Vol. 42, 2010, pp. 531-555.

[4]Guildenbecher, D. R., Gao, J., Reu, P. L., and Chen, J. "Digital holography simulations and experiments to quantify the accuracy of 3D particle location and 2D sizing using a proposed hybrid method," *Applied Optics* Vol. 52, No. 16, 2013, pp. 3790-3801.

[5]Gao, J., Guildenbecher, D. R., Reu, P. L., and Chen, J. "Uncertainty characterization of particle depth measurement using digital in-line holography and the hybrid method," *Optics Express* Vol. 21, No. 22, 2013, pp. 26432-26449.

[6]Gao, J., Guildenbecher, D. R., Engvall, L., Reu, P. L., and Chen, J. "Refinement of particle detection by the hybrid method in digital in-line holography," *Applied Optics* Vol. 53, No. 27, 2014, pp. G130-G138.

[7]Guildenbecher, D. R., Reu, P. L., Stauffacher, H. L., and Grasser, T. W. "Accurate measurement of out-of-plane particle displacement from the cross-correlation of sequential digital in-line holograms," *Optics Letters* Vol. 38, No. 20, 2013, pp. 4015-4018.

[8]Guildenbecher, D. R., Engvall, L., Gao, J., Grasser, T. W., Reu, P. L., and Chen, J. "Digital in-line holography to quantify secondary droplets from the impact of a single drop on a thin film," *Experiments in Fluids* Vol. 55, 2014, p. 1670.

[9]Guildenbecher, D. R., Cooper, M. A., Gill, W., Stauffacher, H. L., Oliver, M. S., and Grasser, T. W. "Quantitative, three-dimensional imaging of aluminum drop combustion in solid propellant plumes via digital in-line holography," *Optics Letters* Vol. 39, No. 17, 2014, pp. 5126-5129.

[10]Gao, J., Guildenbecher, D. R., Reu, P. L., Kulkarni, V., Sojka, P. E., and Chen, J. "Quantitative, 3D diagnostics of multiphase drop fragmentation via digital in-line holography," *Optics Letters* Vol. 38, No. 11, 2013, pp. 1893-1895.

[11]Ling, Y., Wagner, J. L., Beresh, S. J., Kearney, S. P., and Balachandar, S. "Interaction of a planar shock wave with a dense particle curtain: Modeling and experiments," *Physics of Fluids* Vol. 24, No. 11, 2012, p. 113301.

[12] Wagner, J. L., Beresh, S. J., Kearney, S. P., Trott, W. M., Castaneda, J. N., Pruett, B. O., and Baer, M. R. "A multiphase shock tube for shock wave interactions with dense particle fields," *Experiments in Fluids* Vol. 52, No. 6, 2012, pp. 1507-1517.

[13] Wagner, J., Beresh, S., DeMauro, E., Casper, K., Pruett, B., and Farias, P. "Time-resolved PIV in a shock tube using a pulse-burst laser," *11th International Symposium on Particle Image Velocimetery*. Santa Barbara, California, 2015.

[14] White, F. M. *Fluid Mechanics*: The McGraw-Hill Companies, 2002.

[15] Kline, S., and McClintock, F. "Describing uncertainties in single-sample experiments," *Mechanical Engineering* Vol. 75, 1953, pp. 3-8.

[16] Guildenbecher, D. R., and Sojka, P. E. "Demonstration of High Speed (20 kHz) Digital Inline Holographic (DIH) Imaging of a Multiphase Event: Drop Impact on a Thin Liquid Film," *ILASS Americas 27th Annual Conference on Liquid Atomization and Spray Systems*. Raleigh, 2015.

[17] O'Rourke, P. J., and Amsden, A. A. "The tab method for numerical calculation of spray droplet breakup," *International Fuels and Lubricants Meeting and Exposition*. SAE Technical Paper Services, Toronto, Ontario, 1987.